RSC Advances




ROYAL SOCIETY OF CHEMISTRY

www.rsc.org/advances

Cite this: DOI: 10.1039/c0xx00000x

www.rsc.org/xxxxxx

ARTICLE TYPE

# Synthesis of mesoporous $TiO_2$@C@$MnO_2$ multi-shelled hollow nanospheres with high rate capability and stability for lithium-ion batteries

**Li Liu,‡[a] Jun Peng,‡[a] Gang Wang[a*], Yanqing Ma[a], Feng Yu[a*], Bin Dai[a], Xu-Hong Guo[a,b] and Ching-Ping Wong[c,d]**

***Received (in XXX, XXX) Xth XXXXXXXXX 20XX, Accepted Xth XXXXXXXXX 20XX***
**DOI: 10.1039/b000000x**

While $TiO_2$ is regarded as a good anode material for Li ion storage because of its excellent cycling stability, high safety and low cost, its practical applications for Li-ion batteries (LIBs) still present a great challenge due to its poor conductivity and low theoretical capacity. Hybrid nanostructured electrode design offers opportunities to circumvent these drawbacks. Herein, we report a cost-effective strategy for the fabrication of mesoporous $TiO_2$@C@$MnO_2$ multi-shelled hollow nanospheres as LIBs anodes. The multiple-shelled structure effectively couple the electrochemical functionality of $TiO_2$, $MnO_2$ and C including: the excellent stability of $TiO_2$, the large capacity of $MnO_2$, and the high electronic conductivity of the carbon layer. Meantime, the mesoporous shells and hollow nanostructure design not only provides fast $Li^+$ transportation throughout the electrode, but also can further buffer the volume expansion of electrodes during charge/discharge. As a result, $TiO_2$@C@$MnO_2$ multi-shelled hollow nanospheres exhibit an enhanced charge/discharge capacity(506.8 mAh $g^{-1}$ at the rate of 0.3C after 100 cycles) and excellent rate performance (278.7 mAh $g^{-1}$ at 3C after 200 cycles), much better than the individual parts. Our work on the hybrid hollow structures with multiple shells demonstrates an efficient way to realize the enhancement of electrochemical performance of LIB anode materials, thus casting light on the development of advanced anode materials for next-generation, high-performance LIBs.

[a] *School of Chemistry and Chemical Engineering, Key Laboratory of Materials-Oriented Chemical Engineering of Xinjiang Uygur Autonomous Region, Shihezi University, Shihezi, P.R. China. Email:gwangshzu@163.com, yufeng05@mail.ipc.ac.cn*
[b] *State Key Laboratory of Chemical Engineering, East China University of Science and Technology, Shanghai 200237, P. R. China*
[c] *Department of Electronic Engineering, The Chinese University of Hong Kong, Shatin, NewTerritories, HongKong, SAR, China*
[d] *School of Materials Science and Engineering, Georgia Institute of Technology, Atlanta, GA, 30332, United States*
‡These authors contributed equally to this work.

Cite this: DOI: 10.1039/c0xx00000x

www.rsc.org/xxxxxx

ARTICLE TYPE

## 1. Introduction

Rechargeable Li-ion batteries (LIBs) are now considered as the most important power sources for various portable electronic devices, electric vehicles (EVs) and hybrid electronic vehicles (HEVs).[1-4] In the past few decades, great efforts have been devoted in search of alternative anode materials to take the place of the commercially used graphite anode to construct high-performance LIBs. Among the available materials, transition metal oxides have long been studied as potential anode materials for LIBs because of the ease of large-scale fabrication and their rich redox reactions involving different ions, which contribute to high specific capacities.[5-7] Transition metal oxide-based anodes can be classified into two main groups depending on their reaction mechanisms:[8-10] (i) insertion/extraction reaction mechanism that involves the insertion and extraction of Li into and from the lattice of the transition metal oxide, and (ii) conversion reaction mechanism that involves the formation and decomposition of Li oxide ($Li_2O$), accompanying the reduction and oxidation of metal nanoparticles. Generally, insertion reaction-based metal oxide anodes only involve less than one electron transfer, leading to good structural stability at the cost of low specific capacity. By contrast, conversion reaction-based metal oxides involve more than one electron transfer in the electrochemical reaction, which deliver high energy density but poor cyclic performance due to huge volume expansion during charge/discharge. Therefore, the independent use of these transition metal oxides is still not satisfactory.

To bridge the performance gap between these materials, attempts at novel electrode design have been extensively made. One promising route is to scrupulously design nanoarchitecture of the electrode materials and smart hybridization with functional synergy, that is, the use of insertion reaction-based metal oxide/conversion reaction-based metal oxide hybrid nanostructures.[11-23] In this regard, the advantages of the high capacity for conversion reaction-based metal oxide and the structural stability of insertion reaction-based metal oxide will be combined together.[24] For example, Yu and co-workers[11] recently reported an efficient strategy for the synthesis of well-ordered hierarchical G-$TiO_2$@$Co_3O_4$ NBs. The as-formed hierarchical G-$TiO_2$@$Co_3O_4$ NBs exhibit highly reversible capacity, excellent cyclability, and good rate capability as anode materials for LIBs. Chen and co-workers[12] successfully synthesized $TiO_2$−C/$MnO_2$ core−double-shell nanowire arrays. The unique $TiO_2$−C/$MnO_2$ core−double-shell nanowires exhibited enhanced electrochemical cycling and rate properties compared to that of the $TiO_2$ and $TiO_2$−C nanowires. Luo and co-workers[13] recently reported a facile and versatile method to fabricate a $TiO_2$@$Fe_2O_3$ core–shell nanostructure that combines hollow and hierarchical features. Such rationally designed LIB anodes exhibit a high reversible capacity (initial value 840 mAh $g^{-1}$), improved cycle stability (530 mAh $g^{-1}$ after 200 cycles at the current density of 200 mA $g^{-1}$), as well as outstanding rate capability. Currently, despite some significant advances already achieved, the deployment of multi-functional hybrid materials based on metal oxide nanostructures is still at its early stage. A key challenge in this direction is to build up an integrated smart architecture, in which structural features and electroactivities of each component are fully manifested, the interface/chemical distributions are homogeneous at a nanoscale and a fast ion and electron transfer is guaranteed.[25]

Hollow micro-/nano-structured materials have been recognized as one type of promising material for applications in energy-related systems, due to their high surface area and short path length for charge transport.[26-40] In particular, complex hollow structures with multiple shells are highly desirable, and can be expected to further tune the properties of materials by manipulating the structure of hollow materials on the micro- and nano-scale, consequently providing even greater performance improvements. Recently, Lou and co-workers[29] reported a universal method for growing mesostructured $TiO_2$ shells on diverse functional particles through a cooperative assembly-directed process. They demonstrated that these mesoporous $TiO_2$ nanoshells as anode materials for LIBs with long-term cycling stability. Xu and co-workers[31] prepared the $Fe_3O_4$@$MnO_2$ ball-in-ball hollow spheres ($Fe_3O_4$@$MnO_2$ BBHs). The as-prepared $Fe_3O_4$@$MnO_2$ BBHs exhibited the merits of excellent catalytic performance, easy separation, good stability and recyclability. Wang and co-workers[32] prepared CuO@NiO microsphere with three-layer ball-in-ball hollow morphology by Cu–Ni bimetallic organic frameworks. This ternary metal oxide hollow structure is found to be very suitable for solving the critical volume expansion problem and a reversible larger-than-theoretical capacity of 1061 mAh·$g^{-1}$ can be retained after a repetitive 200 cycles without capacity fading compared to the initial cycle. However, the design and fabrication of multi-component hierarchical heterostructures with highly-accessible surface areas and fast ion diffusion for LIBs still remains a challenge.

Herein, we report a facile and scalable strategy to obtain mesoporous $TiO_2$@C@$MnO_2$ multi-shelled hollow nanospheres (HNSs) by a two-step layer-by-layer deposition growth process. As an anode material, the designed material has the following advantages: First, the multiple-shelled structure of $TiO_2$, $MnO_2$ and C can effectively couple the electrochemical functionality of the individual components including: the excellent stability of $TiO_2$, the large capacity of $MnO_2$, and the high electronic conductivity of the carbon layer. Second, in situ chemical redox reaction between carbon and $KMnO_4$ to ensure $MnO_2$ nanoparticles homogeneous decoration onto $TiO_2$@C HNSs. Third, mesoporous shells and hollow nanostructure design not only provides fast $Li^+$ transportation throughout the electrode, but also can further buffer the volume expansion of electrode during charge/discharge. Consequently, the $TiO_2$@C@$MnO_2$ multi-shelled HNSs manifested high specific capacity, excellent cycling performance and superior excellent rate capabilities.

## 2. Experimental Methods

### 2.1 Materials preparation

Glucose, cetyltrimethyl ammonium bromide (CTAB), tetrabutyl titanate (TBT), potassium permanganate were purchased from Adamas Reagent. All the chemicals were of analytical grade and used without further purification.

**Synthesis of $TiO_2$ HNSs:** $TiO_2$ HNSs were prepared through a hard-templet method. First, 0.4 g carbon spheres prepared by a previously reported method[41] were dispersed in a solution including 70 mL ethanol, 1mL distilled water with the assistance of ultrasound. Then 1 mL $Ti(OC_4H_9)_4$ (TBT) mixed with 10mL ethanol was added to the black suspension. The mixture was stirred for 1 h at room temperature and transferred to a 100 mL Teflon-lined stainless steel autoclave and maintained at 180 °C for 6 h. After cooling to room temperature, the precipitates were collected by centrifuging, and washed with water and ethanol, and dried in air at 80 °C for 6 h. Finally, the resultant composite was heated to 500 °C in air at a heating rate of 2 °C $min^{-1}$ and held for 6h, yielding a white powdered product ($TiO_2$ HNSs).

**Synthesis of $TiO_2$@C HNSs:** The $TiO_2$@C HNSs were prepared by a glucose-assisted hydrothermal treatment and subsequent heat treatment. In a typical synthesis, 0.2 g of as-synthesized $TiO_2$ HNSs were dispersed in 60 mL of 0.5 M aqueous glucose solution. The suspension was transferred to a 100 mL Teflon-lined autoclave and heated at 180 °C for 3 h. The product was again harvested by centrifugation and washed with ethanol and distilled water for three times, respectively. After drying at 80 °C for 6 h, the resulting brown powder was carbonized at 550 °C for 3 h under Ar atmosphere to obtain $TiO_2$@C HNSs.

**Synthesis of $TiO_2$@C@$MnO_2$ multi-shelled HNSs:** The electro-active $MnO_2$ coatings were decorated onto the $TiO_2$@C HNSs by in situ chemical redox reaction between carbon and $KMnO_4$. Typically, the as-prepared $TiO_2$@C HNSs were dispersed into 30 mL different concentrations of $KMnO_4$ aqueous solution for 18h at room temperature. Subsequently, the as-prepared $TiO_2$@C@$MnO_2$ multi-shelled HNSs were rinsed with deionized water and dried at 100 °C overnight in a vacuum oven.

### 2.2 Materials Characterization

The phase purity and crystal structure of the obtained materials were studied using an X-ray diffraction (XRD, Bruker AXS D8 Advance) system with Cu Kα radiation from 10-80°. Field emission scanning electron microscopy (FE-SEM, LEO FESEM 1530), transmission electron microscopy (TEM, JEOL 2010F, equipped with energy dispersive X-ray spectroscopy (EDS)) and high-resolution transmission electron microscopy (HRTEM) were used to examine the morphologies, crystalline structures, and element distributions of the samples. Nitrogen adsorption and desorption isotherms were measured at 77 K on a Micromeritics ASAP2010 instrument. Specific surface area calculations were made using the Brunauer-Emmett-Teller (BET) method. The pore size distribution (PSD) curves were calculated from the isotherm using the BJH (Barrett-Joyner-Halenda) algorithm. X-ray photoelectron spectroscopy (XPS, Thermal Scientific K-Alpha XPS spectrometer) was used to investigate the Mn, C, and other element valences in $TiO_2$@C and $TiO_2$@C@$MnO_2$ multi-shelled HNSs. Thermogravimetric analysis (TGA) was carried out on a simultaneous thermal analyzer (NETZSCH STA 449 F3) in an air atmosphere from room temperature to 700 °C at a rate of 10 °C

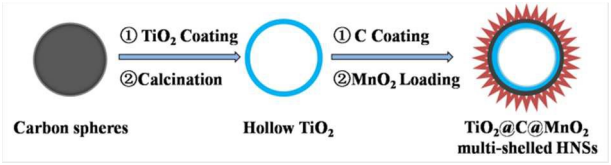


**Figure 1** Schematic illustration of the synthesis process of $TiO_2$@C@$MnO_2$ HNSs.

$min^{-1}$. The relative $MnO_2$ composition of $TiO_2$@C@$MnO_2$ HNSs was determined by an inductively coupled plasma optical emission spectrometer (ICP-OES, IRIS Intrepid II XSP).

### 2.3 Electrochemical Measurement

The electrochemical experiments were performed using 2032-type coin cells, with metallic lithium foil served as the counter electrode. The working electrodes were prepared with active materials, carbon black, and PVDF binder at a weight ratio of 8:1:1 in N-methyl-2 pyrrolidinone (NMP). The obtained slurry was coated onto Cu foil and dried at 120℃ for 12h. The dried tape was then punched into round plates with diameter of 12.0 mm as the cathode electrodes. The loading density of the electrode was about 2 mg $cm^{-2}$. The working electrode and counter electrode were separated by a Celgard 2400 membrane. The electrolyte used was 1 M $LiPF_6$ dissolved in the mixture of ethyl carbonate (EC), dimethyl carbonate (DMC) and ethylmethyl carbonate (EMC) with the volume ratio of 1:1:1. The assembly of the cell was conducted in an Ar-filled glove box ($H_2O$ and $O_2$<1ppm) followed by an overnight aging treatment before the test. Galvonostatic charge–discharge was measured on a LAND battery tester (LAND CT 2001A, China) in the voltage window of 0.01-3.0 V versus $Li^+$/Li. All of the specific capacities here were calculated on the basis of the total weight of active materials. Cyclic voltammetry (CV) and electrochemical impedance spectroscopy (EIS) were measured using a potentiostat (CHI 604C, CH Instrumental Inc.). The impedance spectra were carried out in the frequency range from 100 kHz to 0.01Hz.

## 3. Results and Discussion

Figure 1 shows the formation process of the $TiO_2$@C@$MnO_2$ multi-shelled HNSs. First, amorphous carbon nanospheres are prepared by a facile modified hydrothermal process, according to previous work.[41] Then, $TiO_2$ HNSs are prepared by coating precursor of $TiO_2$ on carbon spheres template, followed by calcination. The carbon layers were then coated on the shells of $TiO_2$ HNSs via a glucose-assisted hydrothermal treatment, and subsequent heat treatment. Finally, the carbon layer deposited onto $TiO_2$ HNSs as an interfacial reactive template to grow $MnO_2$ nanostructures, based on a green reaction between $KMnO_4$ and carbon: $4MnO_4^- + 3C + H_2O = 4MnO_2 + CO_3^{2-} + 2HCO_3^-$. The carbon coating not only confines the $MnO_2$ growth reaction specifically to the HNSs surface, giving rise to well-constructed hybrid architectures, but also the remaining carbon layer can significantly enhances electron transport throughout the composite materials.

We first employ field-emission scanning electron microscopy (FESEM) and transmission electron microscopy (TEM) to examine the structure and morphology of $TiO_2$ HNSs and

$TiO_2$@C HNSs. From the FESEM image (Figure 2a, b), we can find that these two samples are almost the same and are composed of nanospheres. Their hollow structures can be confirmed by the TEM images (Figure 2c, d). The average diameter of these HNSs is about 250 nm with a shell thickness of approximately 40 nm (Figure S1a and Figure S2a, ESI†). Obviously, these shells are composed of small nanocrystals (<10 nm) and exhibit a mesoporous structure (Figure S1b and Figure S2b, ESI†). The HRTEM of $TiO_2$@C HNSs shown in Figure 2e clearly displays the lattice fringes of anatase $TiO_2$, indicating the highly crystalline nature of $TiO_2$ in the $TiO_2$@C HNSs. The interplanar distance between the lattice fringes is 0.35 nm, which can be indexed to the (101) crystal plane of anatase $TiO_2$. Meanwhile, the carbon coating with a thickness of ca. 2~3 nm was found to be deposited on the surface of $TiO_2$ crystallites, confirming the formation of $TiO_2$@C HNSs. Thermogravimetric analysis of $TiO_2$@C HNSs (Figure S3, ESI †) revealed that the weight fraction of carbon in the HNSs was 6.5 wt%, according to the remaining weight of $TiO_2$. The selected-area electron diffraction (SAED) pattern (Figure 2f) with clear diffraction rings, corresponding to (101), (004) and (200) of randomly oriented anatase $TiO_2$, further confirms the high crystallinity of $TiO_2$ in $TiO_2$@C HNSs.

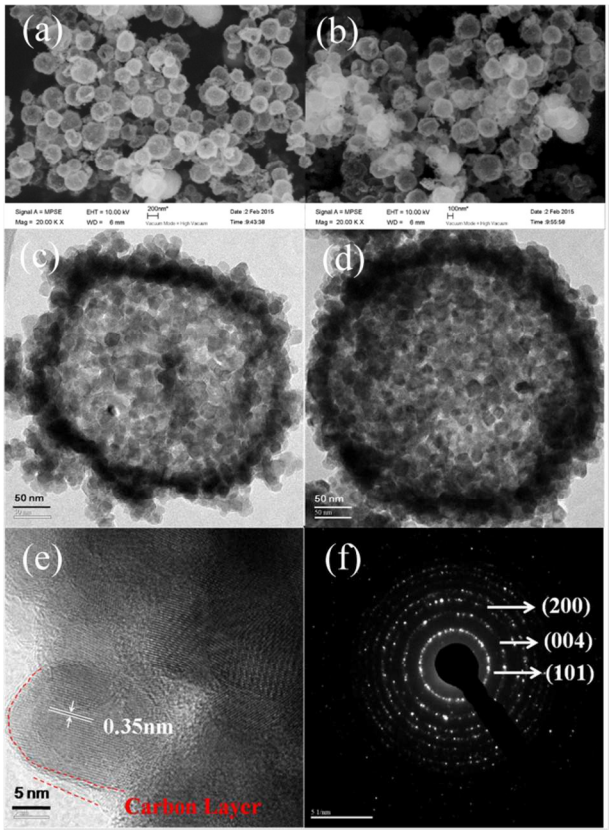


**Figure 2** Morphology characterizations of $TiO_2$ HNSs and $TiO_2$@C HNSs. FESEM image of (a) $TiO_2$ HNSs and (b) $TiO_2$@C HNSs; TEM image of (c) $TiO_2$ HNSs and (d) $TiO_2$@C HNSs; (e) HRTEM image of a single $TiO_2$@C HNSs; (f) Selective Area Electron Diffraction pattern of $TiO_2$@C HNSs

Further morphological and microstructural characterizations of the $TiO_2$@C@$MnO_2$ multi-shelled HNSs were performed using FESEM and TEM as shown in Figure 3. From the FESEM image in Figure 3a, it can be seen that the spherical structure is preserved after the $MnO_2$-coating process. The broken spheres reveal that the nanospheres appear as hollow interior (insert in Figure 3a). TEM image (Figure 3b) suggests that these composite spheres are composed of hollow interior (200-300 nm). From the magnified TEM images (Figure 3c,d), it can be seen that the surface of the spheres form a lot of whistler due to the deposition of $MnO_2$. More importantly, the shells of $TiO_2$@C@$MnO_2$ multi-shelled HNSs still keep the porous structure (Figure S4, ESI†). The HRTEM of $TiO_2$@C@$MnO_2$ multi-shelled HNSs (Figure 3f) further confirm the $MnO_2$ coating layers have not clear lattice fringes, indicating poor crystallinity. Moreover, in comparison with the SAED pattern of $TiO_2$@C HNSs, the SAED pattern of $TiO_2$@C@$MnO_2$ multi-shelled HNSs (Figure 3e) appears as slightly reduced crystallinity, which can stemmed largely from the formation of poor crystalline $MnO_2$ coating layer. The $MnO_2$ content in the $TiO_2$@C@$MnO_2$ multi-shelled HNSs, which is determined by inductively coupled plasma optical emission spectrometer (ICP-OES), is 17.8 wt% (Table S1b, ESI†).

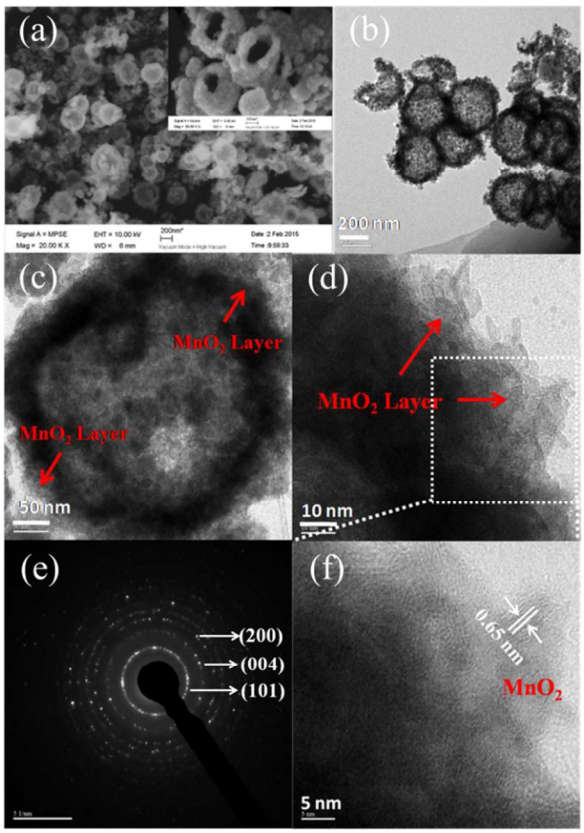


**Figure 3** Morphology characterizations of $TiO_2$@C@$MnO_2$ HNSs. (a) FESEM image; (b) TEM image; (c,d) magnified TEM image of a single $TiO_2$@C@$MnO_2$ HNSs; (e) Selective Area Electron Diffraction pattern; (f) HRTEM image of the $MnO_2$ particles in $TiO_2$@C@$MnO_2$ HNSs.

Energy-dispersive X-ray spectrometry (EDS) mapping images of a single $TiO_2$@C@$MnO_2$ multi-shelled HNSs (Figure 4) unambiguously confirm the structure of the $TiO_2$@C@$MnO_2$ multi-shelled HNSs. It is worth mentioning that the distribution of Ti element is sandwiched between the inner and outer Mn element, indicating that $TiO_2$ shell is wrapped in the inner and outer $MnO_2$ layers. Carbon elemental mapping image also manifest that carbon is evenly distributed in the shell of the hollow sphere (Figure 4d). These carbon shells will provide as a

conductive medium to improve the conductivity of

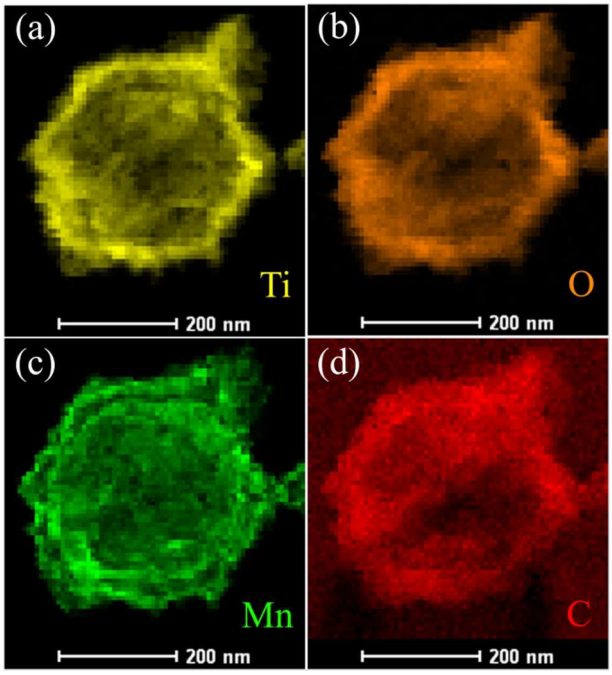


**Figure 4** EDS mapping of Ti (a), O (b), Mn (c), and C (d) from TiO2@C@MnO2 HNSs.

$TiO_2$@C@$MnO_2$ multi-shelled HNSs. Thus, the multi-shelled and hollow structure is expected to contribute to the high capability and cyclic stability of the resulting $TiO_2$@C@$MnO_2$ multi-shelled HNSs as an anode for lithium ion batteries.

XRD measurements were conducted to determine the phase structure of the as-prepared HNSs and are shown in Figure 5a. It can be seen that the $TiO_2$ HNSs can be indexed to the anatase structure phase (JCPDS No. 65-2900). The diffraction peaks of $TiO_2$@C HNSs after a carbon coating treatment have a consistent position with pure $TiO_2$ HNSs. The constant peak position indicates the phase structure of $TiO_2$ has not been changed through the carbon coating process. Furthermore, the carbon coating process did not provide any morphological transformations as demonstrated by SEM and TEM results (Figure 2). After the second layer-by-layer deposition involving the deposition of $MnO_2$ nanoparticles, the XRD pattern of $TiO_2$@C@$MnO_2$ multi-shelled HNSs still only demonstrates the characteristic anatase $TiO_2$ phase. This is most likely due to the poor crystallinity of nanosized $MnO_2$ particles, consistent with the observed result of HRTEM (Figure 3f).

Figure 5b compares the XPS survey spectrum of the $TiO_2$@C HNSs and $TiO_2$@C@$MnO_2$ multi-shelled HNSs in the region of 0-800 eV. Compared with the $TiO_2$@C HNSs, in the XPS survey spectrum of the $TiO_2$@C@$MnO_2$ multi-shelled HNSs, the characteristic peak of Mn appear while the characteristic peak of Ti almost completely disappears after the redox deposition of $MnO_2$, which further indicates that the $TiO_2$ core has been fully coated. Figure 5c further shows the C1s peak from XPS, which corresponds to the carbon layers in the $TiO_2$@C HNSs and $TiO_2$@C@$MnO_2$ multi-shelled HNSs. It can be seen that the characteristic C1s peak of $TiO_2$@C@$MnO_2$ multi-shelled HNSs has the same position as $TiO_2$@C HNSs, but shows decreased peak intensity. The intensity decrease can be explained by the formation of a layer of $MnO_2$ nanoparticles on the surface of

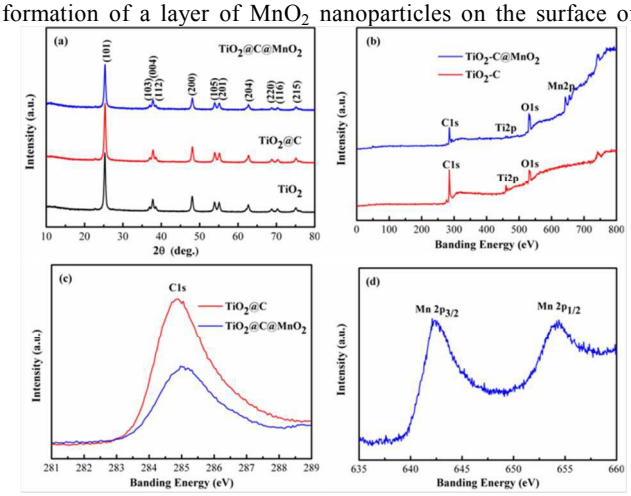


**Figure 5** (a) XRD patterns of $TiO_2$, $TiO_2$@C, and $TiO_2$@C@$MnO_2$ HNSs; (b) XPS survey spectrum of $TiO_2$@C and $TiO_2$@C@$MnO_2$ HNSs ; (c) XPS peaks of C1s of $TiO_2$@C and $TiO_2$@C@$MnO_2$ HNSs, and (d) XPS peaks of Mn2p of $TiO_2$@C@$MnO_2$ HNSs.

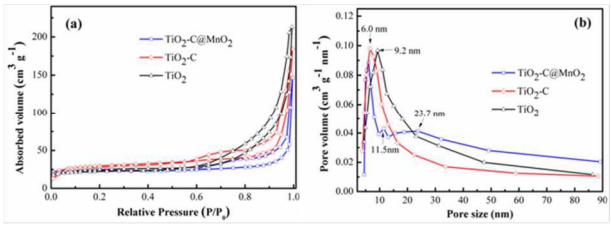


**Figure 6** (a) $N_2$ adsorption/desorption isothermals of $TiO_2$, $TiO_2$@C and $TiO_2$@C @$MnO_2$ HNSs; (b) size distributions of $TiO_2$, $TiO_2$@C and $TiO_2$@C @$MnO_2$ HNSs.

$TiO_2$@C HNSs which reduced the amount of carbon due to the redox reaction with $KMnO_4$. The XPS spectra of Mn 2p of $TiO_2$@C@$MnO_2$ multi-shelled HNSs (Figure 5d) show the peaks of $Mn2p_{3/2}$ and $Mn2p_{1/2}$ centered at 642.1 and 653.8eV, respectively. The spin energy separation of 11.7eV is in good agreement with reported data of $Mn2p_{3/2}$ and $Mn2p_{1/2}$ in $MnO_2$.[42]

$N_2$ adsorption-desorption isotherms were employed to investigate the possible porous structures of $TiO_2$ HNSs, $TiO_2$@C HNSs and $TiO_2$@C@$MnO_2$ multi-shelled HNSs, and the results are showed in Figure 6a. All samples have an IV-type isotherm curve with a distinct hysteresis loop in the range from 0.6~1.0 $P/P_0$, which is indicative of mesoporous materials.[43] The pore size distribution plots are calculated from the desorption isotherm using the Barrett-Joyner-Halenda (BJH) model and are presented in Figure 6b. As been shown in Figure 6b, the dominant pore size of $TiO_2$ HNSs is 9.2 nm. After carbon coating, the dominant pore size of $TiO_2$@C HNSs decreases from 9.2 nm to 6.0 nm, suggesting that carbon fills the porous shell of $TiO_2$ HNSs and form smaller pore. It should be noted that the deposition of $MnO_2$ further decreases the main pores to 5.9 nm. Meantime, some larger pores (~23.7 nm) appear. This can be ascribed to the result of the packing of ultrathin $MnO_2$ nanosheets. As a result, the BET surface areas of $TiO_2$@C HNSs and $TiO_2$@C@$MnO_2$ multi-shelled HNSs are 126.4 $m^2 g^{-1}$ and 139.7 $m^2 g^{-1}$, which are much higher than that of $TiO_2$ HNSs (66 $m^2 g^{-1}$), further indicating the porous structures of the carbon shells and the $MnO_2$ shells. These small pore canals will be propitious to the infiltration of the

electrolyte and provide effective diffusion channels for $Li^+$ in the

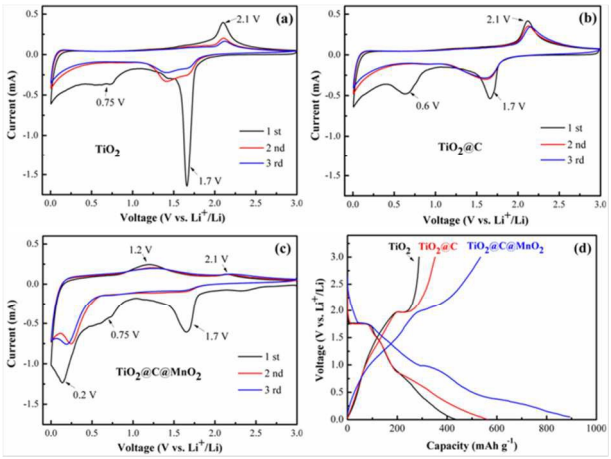


**Figure 7** CV curves of (a) $TiO_2$, (b) $TiO_2$@C, and (c) $TiO_2$@C@$MnO_2$ electrodes at a scan rate of 0.1 mV $s^{-1}$ between 0.01 and 3 V and (d) charge−discharge curves of $TiO_2$, $TiO_2$@C, and $TiO_2$@C@$MnO_2$ electrodes at 0.3C.

charge/discharge process, which may be helpful for improving the diffusion of $Li^+$.

The electrochemical properties of the as-synthesized $TiO_2$ HNSs, $TiO_2$@C HNSs, and $TiO_2$@C@$MnO_2$ multi-shelled HNSs as Li-ion battery anode were investigated using a two-electrode cell with lithium metal as the counter electrode. Figure 7(a-c) compare the cyclic voltammograms (CVs) of the as-synthesized $TiO_2$ HNSs, $TiO_2$@C HNSs, and $TiO_2$@C@$MnO_2$ multi-shelled HNSs electrode cycled between 0.01 and 3.0 V (vs $Li^+$/Li) at a scan rate of 0.2 mV $s^{-1}$. The CV profiles of the $TiO_2$ HNSs and $TiO_2$@C HNSs electrodes are similar and show a pair of cathodic/anodic peaks at around 2.1/1.7 V (vs $Li^+$/Li), which might be related to the lithium storage mechanism between tetragonal anatase $TiO_2$ and orthorhombic $Li_xTiO_2$ ($TiO_2 + xLi^+ + xe^- \leftrightarrow Li_xTiO_2$).[9,16,44,45] Moreover, a broad cathodic peak appear at about 0.6 V (vs $Li^+$/Li), which disappears in the subsequent cycles, indicating the occurrence of some irreversible processes in the electrode materials in the first cycle because of the formation of a solid electrolyte interphase (SEI) film. For the $TiO_2$@C@$MnO_2$ multi-shelled HNSs electrode, the main cathodic peak at 0.2 V (vs $Li^+$/Li) with a abroad shoulder at around 0.5-0.9 V (vs $Li^+$/Li) is assigned to the formation of a SEI layer and the reduction of $MnO_2$, which can be described as $MnO_2 + 4Li^+ + 4e^- \rightarrow Mn(0) + 2Li_2O$.[12,46,47] The anodic peak at around 1.3 V (vs $Li^+$/Li) is attributed to the oxidation of Mn. In addition, the redox peaks of ~1.7 and ~2.1 V (vs $Li^+$/Li) are also observed and can be assigned to $Li^+$ reacts with anatase $TiO_2$.

Figure 7d compares the first discharge/charge profiles of the pristine $TiO_2$ HNSs, $TiO_2$@C HNSs and $TiO_2$@C@$MnO_2$ multi-shelled HNSs electrodes in the voltage range of 0.01-3 V (vs $Li^+$/Li) at a current density of 0.3C (1 C = 335 mA $g^{-1}$). It is evident that a discharge plateau at around 1.7 V (vs $Li^+$/Li) and a charge plateau at around 2.0 V (vs $Li^+$/Li) are observed in all three electrodes due to the $Li^+$ insertion/extraction reaction with anatase $TiO_2$ crystal phase. Meantime, a inclined discharge plateau also is observed at about 1.0~0.5V (vs $Li^+$/Li) in all three electrodes, which can be ascribed to the formation of a SEI layer. Different from the $TiO_2$ HNSs and $TiO_2$@C HNSs, for the $TiO_2$@C@$MnO_2$ multi-shelled HNSs electrode, the third

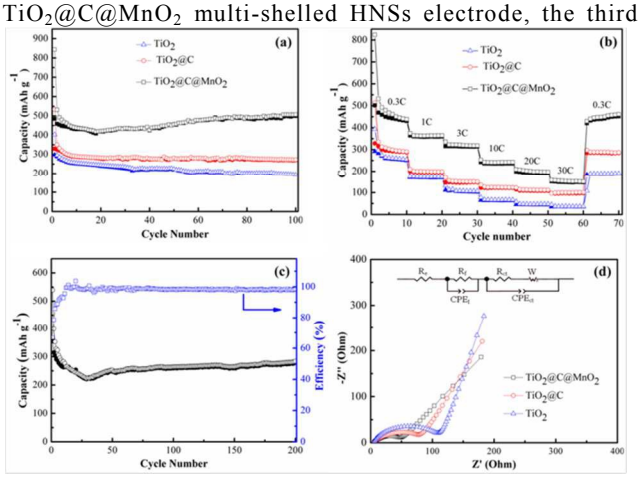


**Figure 8** (a) Comparative cycling performance of $TiO_2$, $TiO_2$@C, and $TiO_2$@C@$MnO_2$ electrodes at a current density of 0.3C; (b) the rate capability of these three electrodes at different current densities; (c) discharge/charge capacities and corresponding coulombic efficiency versus cycle number of the $TiO_2$@C@$MnO_2$ electrode at rates of 3C for 200 cycles; (d)Nyquist plots of the $TiO_2$, $TiO_2$@C, and $TiO_2$@C@$MnO_2$ after 5 cycles in the frequency range from 100 kHz to 0.01 Hz

discharge plateau at around 0.4 V (vs $Li^+$/Li) verified the conversion reactions of $MnO_2$ nanoparticles to Mn metal with $Li_2O$ formation, which is commonly observed for a variety of transition-metal oxide electrode materials.[13,48-50] These plateau voltages in the first cycle were in good agreement with the oxidation and reduction peaks in the above mentioned CVs. The initial discharge and charge capacities gradually increased from 403.5 and 297.4 mAh $g^{-1}$ of $TiO_2$ HNSs to 533.4 and 338.7 mAh $g^{-1}$ of $TiO_2$@C HNSs, and finally to 843.6 and 504.9 mAh $g^{-1}$ of $TiO_2$@C@$MnO_2$ multi-shelled HNSs. The increased capacity can be attributed to the combination effects of carbon coating and $MnO_2$. A large irreversible capacity is observed in the first cycle not only for $TiO_2$ HNSs (columbic efficiency 73.7%) and $TiO_2$@C HNSs (columbic efficiency 63.5%) but also for $TiO_2$@C@$MnO_2$ multi-shelled HNSs (columbic efficiency 59.8%). This can be due to the $Li^+$ storage in the irreversible sites and the formations of a SEI layer.[12,] In addition, the adsorbed moisture in the mesoporous samples will cause the decomposition of the electrolyte, which also gives rise to some irreversible capacity.[51,52] The smaller initial columbic efficiency of $TiO_2$@C@$MnO_2$ multi-shelled HNSs may be due to the in situ formation of highly reactive metallic Mn nanograins at low potentials promoting the growth of SEI film.

The cycling performance for these three samples are compared to further illustrate the superior cycling performance of the $TiO_2$@C@$MnO_2$ multi-shelled HNSs electrode. Figure 8a shows the charge/discharge capacities versus cycle number of the pristine $TiO_2$ HNSs, $TiO_2$@C HNSs and $TiO_2$@C@$MnO_2$ multi-shelled HNSs at a current density of 0.3C up to 100 cycles. It can be seen that the $TiO_2$@C HNSs electrode exhibits superior cycling stability with a discharge capacity of 272.6 mAh $g^{-1}$ after 100 cycles, which correspond to 77.8% retention of second discharge capacity. Although the $TiO_2$ HNSs electrode delivers almost the same capacity as the $TiO_2$@C HNSs in the first few cycles, it exhibit gradual capacity decrease to 192.7 mAh $g^{-1}$ after 100 cycles, only corresponding to 65.2% retention of second

discharge capacity. The capacity difference between the $TiO_2$ HNSs and $TiO_2$@C HNSs imply that the carbon layers on the surface of the $TiO_2$@C HNSs play an essential role in improving the cyclic performance. It should be emphasized that, the $TiO_2$@C@$MnO_2$ multi-shelled HNSs electrode inherits the superior cyclability of $TiO_2$@C HNSs electrode, but also delivers higher capacity than $TiO_2$@C HNSs electrode due to the $MnO_2$ layer capable of contributing high capacity. Its discharge capacity decreases rapidly to 419.5 mAh $g^{-1}$ in the initial 19 cycles, and then increases significantly over 506.8 mAh $g^{-1}$ even after 100 cycles, corresponding to 95.3% retention of second discharge capacity. Similar phenomena have been reported for various metal oxide anodes.[53-55] In general, the capacity fade for metal oxide anodes should be attributed to the pulverization of original aggregation of metal oxide particles during the $Li^+$ intercalation/extraction process, leading to the loss of electrical connectivity between the particles and current collector. In the case of the $TiO_2$@C@$MnO_2$ multi-shelled HNSs electrode, with the aid of the $TiO_2$ backbone, the dissolution and mechanical failure of the exterior $MnO_2$ particles can be effectively prevented or relieved. After that, the increase of capacity could be ascribed to the reversible growth of a polymeric/gel-like film around the active materials caused by the decomposition of the electrolyte at a low potential, which enabled the mechanical cohesion and delivered excess capacity through a so-called "pseudo-capacity-type" behavior.[53,54] To further illustrate the effect of the $TiO_2$@C backbone, the cycling performance of the bare $MnO_2$ HNSs is shown in Figure S4 (shown in the ESI†). The specific capacities of the bare $MnO_2$ HNSs electrode show a continuous decline, and decrease from the initial 1678.4 mAh $g^{-1}$ to 224.6 mAh $g^{-1}$ after 80 cycles. This result indicates that the $TiO_2$@C backbone can remarkably improve the cyclability of $MnO_2$. We also studied the charge–discharge performance of other $TiO_2$@C@$MnO_2$ multi-shelled HNSs samples with different $MnO_2$ contents (Figure S5, ESI†). The result verifies again that incorporation of $MnO_2$ indeed improves the capacity of these $TiO_2$-based materials. But too much of $MnO_2$ (e.g. 29.7 wt%) seems to be of no benefit for obtaining better electrochemical performance, owing to the destruction of the electrode structure during charge/discharge process (Figure S6, ESI†).

More importantly, the $TiO_2$@C@$MnO_2$ multi-shelled HNSs electrode exhibits a much better rate performance. Figure 8b compares the charging/discharging behavior of $TiO_2$ HNSs, $TiO_2$@C HNSs and $TiO_2$@C@$MnO_2$ multi-shelled HNSs at different C rates ranging from 0.3 to 30 C. From the rate capability shown in Figure 8b, it is observed that the $TiO_2$@C@$MnO_2$ multi-shelled HNSs electrode achieves reversible capacities of 364.5, 318, 242.5, 196.9, and 149.9 mAh $g^{-1}$ at the current densities of 1C, 3C, 10C, 20C and 30C, respectively, which are obviously higher than those of $TiO_2$ HNSs and $TiO_2$@C HNSs at the corresponding densities. It is noted that, when the current density was recovered to 0.3C after the rate performance test, the reversible capacities of all these samples returned back to their initial value approximately except for the $TiO_2$@C@$MnO_2$ multi-shelled HNSs electrode, which reached ca. 461.1 mA h $g^{-1}$, higher than the value (438.3 mAh $g^{-1}$) acquired at the initial density of 0.3C, suggesting that the high current charge/discharge process not only did little to break down the integrity of the electrode, but also led to a gradual activation of the electrode material, which has also been found in other anode nanomaterials.[13,56,57] To further understand the satisfactory electrochemical performance, a TEM image of the $TiO_2$@C@$MnO_2$ multi-shelled HNSs after the rate cycling test is presented in Figure S7 (shown in the ESI†). In addition to some impurities from carbon black, the HNSs in the $TiO_2$@C@$MnO_2$ multi-shelled HNSs could be easily identified after long-term repeated lithiation/delithiation, which indicates the excellent structure stability of the $TiO_2$@C@$MnO_2$ multi-shelled HNSs.

In order to further confirm the long-term cycling performances of the $TiO_2$@C@$MnO_2$ multi-shelled HNSs electrode at higher rates, Figure 8c shows the discharge/charge capacities and corresponding coulombic efficiency of the $TiO_2$@C@$MnO_2$ multi-shelled HNSs electrode at rates of 3C for 200 cycles. The discharge capacity of $TiO_2$@C@$MnO_2$ multi-shelled HNSs at 3C delivers a similar activation process to that obtained at 0.3C. It firstly decreases to the low value of 223.7 mAh $g^{-1}$ in the 29 cycle, and then increases up to 284.6 mAh $g^{-1}$ at the 200th cycle, corresponding to 71.2% cycle retention of second discharge capacity. Furthermore, the Coulombic efficiencies remained higher than 97% after the first few cycles. On the basis of the above results, the $TiO_2$@C@$MnO_2$ multi-shelled HNSs electrode exhibits high reversible capacity, excellent cycling stability and long circling life than other samples, confirming that the ternary hybridization of $TiO_2$, $MnO_2$ and carbon is an efficient way to achieve the enhancement of electrochemical performance of $TiO_2$-based anode materials. Simultaneously, the as-prepared $TiO_2$@C@$MnO_2$ multi-shelled HNSs electrode also exhibits comparable capacity retention and cycling performance even at large current density in comparison with recent research studies on the $TiO_2$-based composite anodes for LIBs summarized in Table S2 (shown in the ESI†), including $TiO_2$–C/$MnO_2$ core-double-shell nanowire arrays (218 mAh $g^{-1}$ after 150 cycles at 3350 mA $g^{-1}$),[12] TNAs@$MnO_2$ nanosheet (320 mAh $g^{-1}$ after 100 cycles at 700 mA $g^{-1}$),[53] $TiO_2$-$MnO_2$/$MnO_2$ nanofibers (185 mAh $g^{-1}$ after 400 cycles at 2000 mA $g^{-1}$),[17] $TiO_2$ nanotube @$SnO_2$ nanoflake (450 mAh $g^{-1}$ after 50 cycles at 1600 mA $g^{-1}$),[56] $TiO_2$@$Fe_2O_3$ (430.2 mAh $g^{-1}$ after 103 cycles at 200 mA $g^{-1}$).[54] $TiO_2$@$Fe_2O_3$ core–shell nanostructures (530 mAh $g^{-1}$ after 200 cycles at 200 mA $g^{-1}$).[13] G-$TiO_2$@$Co_3O_4$ (437 mAh $g^{-1}$ after 190 cycles at 100 mA $g^{-1}$).[11] $TiO_2$@ZnO (340.2 mAh $g^{-1}$ after 100 cycles at 200 mA $g^{-1}$).[15] $TiO_2$/$MnTiO_3$@C (402.6 mAh $g^{-1}$ after 300 cycles at 100 mA $g^{-1}$).[19]

In order to understand the reasons for the improved high rate performance, electrochemical impedance spectroscopy (EIS) measurements were carried out for the three hollow spheres based electrodes after the 5th cycle at a current density of 0.3C, and the impedance plots along with the equivalent circuit model are presented in Figure 8d. The Nyquist plots of all three electrodes depict a semicircle at high-medium frequency and an inclined line at low frequency, which correspond to charge transfer and diffusion, respectively. The components of the equivalent circuit include: $R_e$ as the internal resistance of the battery, $R_f$ as the resistance of the SEI film, $R_{ct}$ as the charge transfer resistance, W as the Warburg impedance of Li ion diffusion into the active materials, and CPE is the constant phase-angle element which involves the double layer capacitance. The fitted impedance

parameters are listed in Table S3 in the ESI.† The charge transfer resistance $R_{ct}$ of the $TiO_2$@C@$MnO_2$ HNSs electrode is 51.8 Ω, which are much lower than the corresponding value of the $TiO_2$@C HNSs electrode (81.4 Ω) and $TiO_2$ HNSs electrode (116.9 Ω). This suggests that the $TiO_2$@C@$MnO_2$ multi-shelled HNSs electrode has a faster charge transfer process and undergo a fast Faradaic reaction, which supports the increased high-rate performance of the $TiO_2$@C@$MnO_2$ HNSs anode in comparison to the other two electrodes.

Based on the above-mentioned experimental results, it can be concluded that our mesoporous $TiO_2$@C@$MnO_2$ multi-shelled HNSs display superior electrochemical performance with large reversible capacity, high rate capability, and excellent cycling performance at high rates. These outstanding properties should be attributed to their distinct structure and the synergistic effect between the $TiO_2$, $MnO_2$ and C, which offer the following benefits: (1) the mesoporous shells and hollow structure may ensure the short transport path for both electrons and lithium ions and the high contact interface between the active materials and the electrolyte, leading to fast charge/discharge rates; (2) the $MnO_2$ layers provide high capacity (3) the $TiO_2$ scaffolds with merely 4% volume change can effectively cushion the volume change and structural stress of $MnO_2$ layers, thus preserve the structural integrity of the whole electrode during charge/discharge process; (4) the carbon shells not only facilitates the deposition of $MnO_2$ nanoparticles, but also significantly enhances electron transport throughout the composite materials. Due to the enhanced structural stability and lithium storage capacity and excellent kinetics for lithium ion and charge transport, the electrochemical performance of mesoporous $TiO_2$@C@$MnO_2$ multi-shelled HNSs are thus remarkably improved.

## 4. Conclusions

In summary, mesoporous $TiO_2$@C@$MnO_2$ multi-shelled HNSs were successfully fabricated through a layer-by-layer deposition technique. This unique multi-shelled hollow nanostructure is made of mesoporous $TiO_2$@C HNSs on which $MnO_2$ nanoparticles are homogeneously deposited via in situ chemical redox reaction between carbon and $KMnO_4$ and effectively couple the electrochemical functionality of the individual components including: the excellent stability of $TiO_2$, the excellent capacity of $MnO_2$, and the high electronic conductivity of the carbon layer. As a result, the $TiO_2$@C@$MnO_2$ multi-shelled HNSs electrode exhibits a high charge/discharge capacity and excellent rate performance (278.7 mAh $g^{-1}$ at 3C after 200 cycles). Therefore, the research on the hybrid hollow structures with multiple shells demonstrates an efficient way to realize the enhancement of electrochemical performance of LIB anode materials, thus casting new light on the development of advanced anode materials for next-generation, high-performance LIBs.

## Acknowledgments

This work was financially supported by Program for Changjiang Scholars and Innovative Research Team in University (PCSIRT, No. IRT1161) and Program of Science and Technology Innovation Team in Bingtuan (No 2011CC001) and the National Natural Science Foundation of China (No. 21263021,U1303291).

## Reference

1 B. Dunn, H. Kamath and J. Tarascon, *Science.* 2011, 334, 928-935.
2 J. B. Goodenough, *Acc. Chem. Res.,* 2013, 46, 1053-1061.
3 M. Armand and J. M. Tarascon, *Nature,* 2008, 451, 652-657.
4 H. Jiang, H. Zhang, Y. Fu, S. Guo, Y. Hu, L. Zhang, Y. Liu, H. Liu and C. Li, *ACS Nano*, 2016, 10, 1648–1654.
5 H. B. Wu, J. S. Chen, H. H. Hng and X. W. Lou, *Nanoscale,* 2012, 4, 2526-2542.
6 J. Ji, J. Liu, ,L. Lai, ,X. Zhao, Y. Zhen, J. Lin, Y. Zhu, H. Ji, L. L. Zhang and R. S. Ruoff, *ACS Nano*, 2015, *9*, 8609-8616.
7 Z. Fan, J. Liang, W. Yu, S. Ding, S. Cheng, G. Yang, Y. Wang, Y. Xi, K. Xi and R. V. Kumar, *Nano Energy,* 2015, 16, 152-162.
8 S. Goriparti, E. Miele, F. D. Angelis, E. D. Fabrizio, R. P. Zaccaria, and C. Capiglia, *J. Power Sources,* 2014, 257, 421-443.
9 C. Zhu, X. Xia, J. Liu, Z. Fan, D. Chao, H. Zhang and H. J. Fan, *Nano Energy,* 2014, 4, 105-112.
10 Z. X. Yang, Q. Meng, Z. P. Guo, X. B. Yu, T. L. Guo and R. Zeng, J. *Mater. Chem. A,* 2013, 1, 10395-10402.
11 Y. Luo, J. Luo, W. Zhou, X. Qi, H. Zhang, Y. Denis, C. M. Li, H. J. Fan and T. Yu, *J. Mater. Chem. A,* 2013, 1, 273-281.
12 J.Y. Liao, D. Higgins, G. Lui, V. Chabot, X. C. Xiao and Z. W. Chen, *Nano Lett.,* 2013, 108, 104-110.
13 J. S. Luo, X. H. Xia, Y. S. Luo, C. Guan, H. Zhang and H. J. Fan, *Adv. Energy Mater.,* 2013, 3, 737-743.
14 X. Q. Chen, H. B. Lin, X. W. Zheng, X. Cai, P. Xia, Y. M. Zhu, X. P. Li and W. S. Li, *J. Mater. Chem. A,* 2015, 3, 18198-18206.
15 L. Gao, S. H. Li, D. K. Huang, Y. Shen and M. K. Wang, *Electrochim. Acta,* 2015, 182, 529-536.
16 Q. H. Tian, Z. X. Zhang, L. Yang and S. I. Hirano, *J. Power Sources,* 2015, 279, 528-532.
17 X.Y. Li, Y.M. Chen, H.M. Yao, X.Y. Zhou, J. Yang, H.T. Huang, Y.W. Mai and L.M. Zhou, *RSC Adv.,* 2014, 4, 39906-39911.
18 C. Zhu, X. Xia, J. Liu, Z. Fan, D. Chao, H. Zhang and H. J. Fan, *Nano Energy,* 2014, 4, 105-112.
19 S. Li, M. Ling, J. X. Qiu, J. S. Han and S. Q. Zhang, *J. Mater. Chem. A,* 2015, 3, 9700-9706.
20 Z. T. Li, Y. K. Wang, H. D. Sun, W. T. Wu, M. Liu, J. Y. Zhou, G. L. Wu and M. B. Wu, *J. Mater. Chem. A,* 2015, 3, 16057-16063
21 H. G. Wang, Y. H. Li, W. Q. Liu, Y. C. Wan, Y. W. Li and Q. Duan, *RSC Adv.,* 2014, 4, 23125-23130.
22 L. Pan, X. D. Zhu, X. M. Xie and Y. T. Liu, *Adv. Funct. Mater.,* 2015,25,3341-3350.
23 X. D. Li, W. Li, M. C. Li, P. Cui, D. H. Chen, T. Gengenbach, L. H. Chu, H. Y. Liu and G. S. Song, *J. Mater. Chem. A,* 2015, 3, 2762-2769.
24 H. Jiang, C. Li, T. Sun and J. Ma, *Chem. Commun.,* 2012,48, 2606-2608.
25 J. Liu , J. Jiang , C. Cheng , H. Li , J. Zhang , H. Gong and H. J. Fan, *Adv. Mater.,* 2011, 23, 2076-2081.
26 M. Yang, Y. Zhong, J. Bao, X. Zhou, J. Wei and Z. Zhou, *J. Mater. Chem. A,* 2015,3, 11387-11394.
27 Z. Y. Wang, L. Zhou and X. W. Lou, *Adv. Mater.,* 2012, 24, 1903-1911.
28 X. Lai, J. E. Halpert and D. Wang, *Energy Environ. Sci.,* 2012, 5, 5604-5618.
29 B. Y. Gan, L. Yu, J. Li and X. W. Lou, *Sci. Adv.,* 2016, 2, 10.1126/sciadv.1501554.
30 L. Yu, B. Y. Guan, W. Xiao and X. W. Lou, *Adv. Energy Mater.,* 2015, 21, 10.1002/aenm.201500981.
31 S. W. Zhang, Q. H. Fan, H. H. Gao, Y. S. Huang, X. Liu, J. X. Li, X. J. Xu and X. K. Wang, *J. Mater. Chem. A,* 2016, 4, 1414-1422.
32 W. Guo, W. Sun, and Y. Wang, *ACS Nano,* 2015, 9, 11462-11471.
33 H. Ren, R. B. Yu, J. Y. Wang, Q. Jin, M. Yang, D. Mao, D. Kisailus, H. J. Zhao, and D. Wang, *Nano Lett.,* 2014, 14, 6679-6684.
34 G. Q. Zhang, H. B. Wu, T. Song, U. Paik and X. W. Lou, *Angew. Chem. Int. Ed.,* 2014 , 53 , 12590-12593.

35 D. Wang, H. He, L. Han, R. Lin, J. Wang, Z. Wu, H. Liu, and H. L. Xin, *Nano Energy,* 2016, 20, 212-220.

36 B. Zhao, S. Y. Huang, T. Wang, K. Zhang, M. M. F. Yuen, J. B. Xu, X. Z. Fu, R. Sun, and C. P. Wong, *J. Power Sources,* 2015, 298, 83-91.

37 G. D. Park, J. S. Cho, and Y. C. Kang, *ACS Appl. Mater. Interfaces*, 2015, 7, 16842-16849.

38 Z. Zhang, Y. Ji, J. Li, Q. Tan, Z. Zhong, and F. Su, *ACS Appl. Mater. Interfaces*, 2015, 7, 6300-6309.

39 G. Q. Zhang, and X. W. Lou, *Angew. Chem. Int. Ed.,* 2014, 53, 9041-9044.

40 X. Wang, X.-L. Wu, Y.-G. Guo, Y. Zhong, X. Cao, Y. Ma and J. Yao, *Adv. Funct. Mater.,* 2010, 20, 1680-1686.

41 L. C. Liu, Q. Fan, C. Z. Sun, X. R. Gu, H. Li, F. Gao, Y. F. Chen and L. Dong, *J. Power Sources,* 2013, 221, 141-148.

42 L. Q. Mai, F. Dong, X. Xu, Y. Z. Luo, Q. Y. An, Y. L. Zhao, J. Pan, and J. N. Yang, *Nano Lett.,* 2013, 13, 740-745.

43 J. Peng, G. Wang, Y. T. Zuo, G. Li, F. Yu, B. Dai and X. H. Guo, *RSC Adv.,* 2016, 6, 20741-20749.

44 J. Qiu, P. Zhang, M. Ling, S. Li, P. Liu, H. Zhao, and S. Zhang, *ACS Appl. Mater. Interfaces,* 2012, 4, 3636-3642.

45 Y. Fan, N. Zhang, L. Zhang, H. Shao, J. Wang, J. Zhang, and C. Cao, *Electrochim. Acta,* 2013, 94, 285-293.

46 A. Yu, H. W. Park, A. Davies, D. C. Higgins, Z. Chen, and X. Xiao, *J. Phys. Chem. Lett.,* 2011, 2, 1855-1860.

47 H. Lai, J. X. Li, Z. G. Chen, and Z. G. Huang, *ACS Appl. Mater. Interfaces,* 2012, 4, 2325-2328.

48 Y. Luo, J. Luo, W. Zhou, X. Qi, H. Zhang, D. Y. W. Yu, C. M. Li, H. J. Fan and T. Yu, *J. Mater. Chem. A,* 2013, 1, 273-281.

49 G. Li, H. Hu, Q. Zhu and Y. Yu, *RSC Adv.,* 2015, 5, 101247-101256.

50 C. He, S. Wu, N. Zhao, C. Shi, E. Liu and J. Li, *ACS Nano,* 2013, 7, 4459-4469.

51 K. Saravanan, K. Ananthanarayanan and P. Balaya, *Energy Environ. Sci.,* 2010, 3, 939-948.

52 X. Yan, Y. J. Li, F. Du, K. Zhu, Y. Q. Zhang, A. Y. Su, G. Chen and Y. J. Wei, *Nanoscale,* 2014, 6, 4108-4116.

53 Q. C. Zhu, H. Hu, G.J. Li, C.B. Zhu and Y. Yu, *Electrochim. Acta,* 2015, 156, 252-260.

54 L. Gao, H. Hu, G. Li, Q. Zhu, and Y. Yu, *Nanoscale,* 2014, 6 , 6463-6467.

55 Z. Wang, D. Luan, S. Madhavi, Y. Hu, and X.W. Lou, *Energy Environ. Sci.,* 2012, 5 , 5252-5256.

56 W. Luo, X. Hu, Y. Sun and Y. Huang, *J. Mater. Chem.,* 2012, 22, 4910-4915.

57 S. M. Guo, J. R. Liu, S. Qiu, W. Liu, Y. R. Wang, N. N. Wu, J. Guo and Z. H. Guo, *J. Mater. Chem. A,* 2015, 3, 23895-23904.

Mesoporous $TiO_2$@C@$MnO_2$ multi-shelled hollow nanospheres (denoted as $TiO_2$@C@$MnO_2$ multi-shelled HNSs) prepared by a layer-by-layer deposition growth process exhibits high high rate capability and stability.